Experimental Investigation and Numerical Modeling of Piezoelectric Bender Element Motion and Wave Propagation Analysis in Soils

Hongwei Liu[a], Giovanni Cascante[b], Pooneh Maghoul[a], Ahmed Shalaby[a]

[a]*Department of Civil Engineering, University of Manitoba, 75A Chancellors Circle, Winnipeg, MB, R3T 5V6, Canada*
[b]*Department of Civil Engineering, University of Waterloo, Waterloo, ON, N2L 3G1, Canada*

Abstract

The bender element (BE) test has been widely used for the characterization of soil specimens to determine the dynamic or low-strain shear modulus. However, the actual behavior of the BE inside the soil specimen still remains unknown. The current ASTM standard does not consider the interference of P waves in BE measurements, which can lead to significant errors in the evaluation of shear wave velocities. In this paper, the BE motion inside different media is numerically studied through a coupled piezoelectric and solid mechanics finite element (FE) model. The numerical results are calibrated and compared with the real motion of the BE monitored using a high-frequency laser vibrometer. The proposed model successfully captured the measured motion of the BE in the air as well as transparent soils. More importantly, the proposed model provided a method for understating the interactions of P waves and S waves in a soil specimen. Simulated signals for an Ottawa sand specimen showed a good agreement with independent results from resonant column tests. The proposed piezoelectric-solid mechanics FE model can be used to study the soil-bender element interaction so that sound recommendations can be given to improve the interpretation of BE tests for different soils.

Keywords: Bender element test, resonant column test, laser vibrometer, wave propagation, solid mechanics, piezoelectric, finite element method

1. Introduction

The dynamic soil properties play an important role in the design of earthquake-resistant structures and foundations. The bender element (BE) test and resonant column (RC) test are the most popular methods used for the evaluation of dynamic soil properties such as the shear wave velocity at low shear strains. The RC test is used to determine the resonant frequency of a soil column, which is related to the shear wave velocity and shear modulus. However, the RC test is time-consuming and costly in comparison to the BE test. The BE utilizes piezo-ceramic materials for the conversion of an electrical signal into mechanical energy. Two bender elements are placed at the two ends of the soil specimen in which one BE is used to introduce a mechanical impulse and the other one is used to receive the propagating pulse (normally in mV). The BE generates not only S-waves in the direction of their plane but also P-waves in the direction normal to their plane. The P-waves reflected from the cell walls can interfere with the generated S-waves [17].

The behavior of the BE has been studied both numerically and experimentally in the literature. Lee and Santamarina [17] showed that the P-wave reflected from the cell wall in the BE test arrives to the BE receiver earlier than the direct S-wave. The interpretation of the BE test results requires the consideration of the geometry of the specimen, such as the radius-to-height ratio [17]. It is found that the resonant frequency of the BE embedded within the soil specimen depends on the stiffness of the BE, soil stiffness, and stress level in the soil [3, 4]. The BE has been used in a triaxial apparatus for the measurement of anisotropy of fine-grained soils [15]; it has shown that the BE is effective in measuring the inherent anisotropy resulting from the plastic strain history. Youn et al. [27] compared the BE test with the resonant column test as well as the torsional shear test in sands; the results

*I am corresponding author
Email addresses: liuh3429@myumanitoba.ca (Hongwei Liu), gcascante@uwaterloo.ca (Giovanni Cascante), pooneh.maghoul@umanitoba.ca (Pooneh Maghoul), ahmed.shalaby@umanitoba.ca (Ahmed Shalaby)

showed that the values of shear wave velocity determined from the BE test correspond well with the resonant column test as well the torsional test in dry conditions [27]. In saturated conditions, however, the BE test tends to overestimate the shear wave velocity in comparison to the two other tests, which is likely due to the S-wave-P-wave interaction [27]. The stiffness of unsaturated soils was tested with the BE and suction-controlled resonant column tests by Hoyos et al. [12]. A good agreement between the BE and resonant column tests was reported in terms of the measurement in stiffness of silty sand under a suction-controlled condition. Gu et al. [11] compared the results of the BE test with the RC test and the cyclic torsional shear test at various confining pressures, densities, and degrees of saturation. It was found that the travel time, under saturated conditions, obtained from the BE test is considerably smaller than that from the RC test due to the dispersion of the S-wave. However, this result could be attributed to the strong participation of p-waves observed in BE tests in saturated media. Recommendations in terms of the selection of the impulse frequency is given to reduce the subjectivity in arrival time of S wave [3]; a single sinusoidal pulse is recommended and the travel length-to-wavelength ratio should be high enough to reduce the near-field effect.

A new BE test setup using a laser vibrometer was used by Irfan et al. [14] to monitor the BE motion inside transparent soils. In this experiment, a transparent granular soil specimen was used, such that the real transmitter response can be measured using the laser vibrometer. The transmitter response inside the soil specimen is very different from the input electrical signal. The BE response is not well represented by a cantilever beam as typically assumed in the literature [16, 17, 28]. The BE was inserted in the water, sucrose solutions, mineral oils, and air to account for the effects of viscosity and density of the fluid medium. Such tests were used for the calibration of the BE transducer. The important findings from such experimental tests are: 1) the input square and step function pulses excite higher modes in comparison to the sine function pulses; 2) the fluid density dominates the transmitter response more than the viscosity of fluid; 3) there are strong p-waves generated in typical BE tests.

Several methods have been developed in the past to interpret the signal obtained through the BE test. The first group is to calculate the shear wave velocity based on the first arrival time, which includes the start-start method, peak-peak method, cross correlation method and cross power method. The cross correlation method is used to measure the degree of correlation of two signals [26] and the cross power method measures the correlation in frequency domain. However, the arrival-time based methods usually results in subjective and inaccurate interpretation of the shear wave velocity. Currently, it is still unclear which method provides the most reliable results [11]. An automatic shear wave velocity estimation method was developed by Finas et al. [9] by applying the Akaike information criteria, which is effective for a signal-to-noise ratio (SNR) smaller than 4. This inherent complexity in the analysis of BE tests is clarified in this paper by the use of calibrated numerical simulations.

The behaviour of the BE has been numerically studied in the literature. Arulnathan et al. [1] used the finite element (FE) method to illustrate that the interpretation of the BE signals based on the cross correlation between the input and output signals is misleading due to the effects of wave interference at the boundaries, the phase lag between the mechanical energy and electrical input and multi-dimensional wave travel issues. A two-dimensional (2D) discrete element method was used by O'Donovan et al. [24] to study the response of an idealised granular material in the BE test. The particle velocity data was used to show the propagation of a central S-wave accompanied by P-waves moving along the sides of the soil specimen. A 2D finite element model was used by Ingale et al. [13] to study the effect of soil types and frequency on BE measurements. It was shown that the FE analysis is consistent with the S-wave velocity obtained through the peak-to-peak method.

An analytical model of piezoelectric BE was developed by Zhou et al. [28] based on the first-order shear deformation theory by assuming a single rotation angle. An analytical modelling approach was also developed based on the beam theory under the quasi-static equilibrium condition, which can be used for the optimized design of piezoelectric bending actuators [7]. A close-form 3D piezoelectric model was developed by Rabbani et al. [25] to investigate the free vibration of piezoelectric hollow cylinder using the transfer matrix method and the state space method.

Despite the above-mentioned efforts, the actual behaviour of the BE inside the soil still remains unknown. Currently, there is no standard interpretation of the BE measurements due to the complex wave interaction introduced by the BE within the soil specimens. In this paper, a piezoelectric-solid mechanics model is proposed to study the BE motion in different media. The model is validated using the BE motion in the air, transparent soil, and Ottawa sand monitored by a laser vibrometer device. The estimation of the soil parameters such as the shear wave velocity and damping ratio of the Ottawa sand using the piezoelectric-solid mechanics model developed in this paper is then compared with independent experimental data obtained via the conventional RC test. Finally, the propagation of P- and S-waves within a soil specimen due to the BE motion is thoroughly studied and the suitability of empirical methods in estimating the S-wave arrival time is discussed.

2. Methodology and Experimental Setup

In this work, a FE model of a BE-soil sample is calibrated and verified using laser vibrometer measurements on a) BE on air, b) BE in transparent soil, and c) BE in Ottawa sand specimen. Then, the results are independently verified using resonant column measurements. The detailed procedure is summarized in Figure 1.

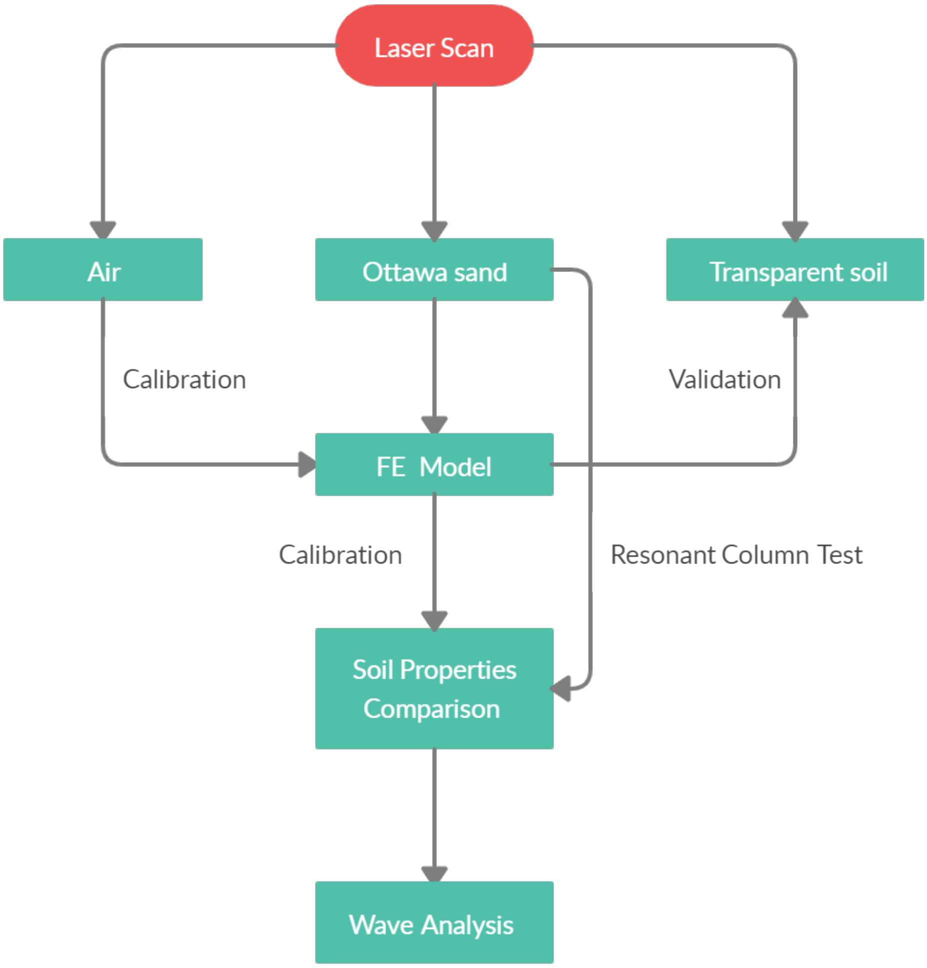

Figure 1: Flowchart of the detailed procedures for the calibration and verification of the BE motion as well as wave analysis within a soil specimen.

2.1. Experimental Setup

A general schematic of the experimental setup is illustrated in Figure 2. The soil specimen is vibrated at the bottom via a piezoelectric BE. The generated P wave and S wave contribute to the overall displacement at the top surface of the soil specimen. The BE motion is then studied through the laser vibrometer readings as well as a piezoelectric-solid mechanics FE modeling using two main soil sample configurations: a) transparent soil to evaluate the BE response and b) an Ottawa sand specimen to evaluate the surface response induced by the

BE.

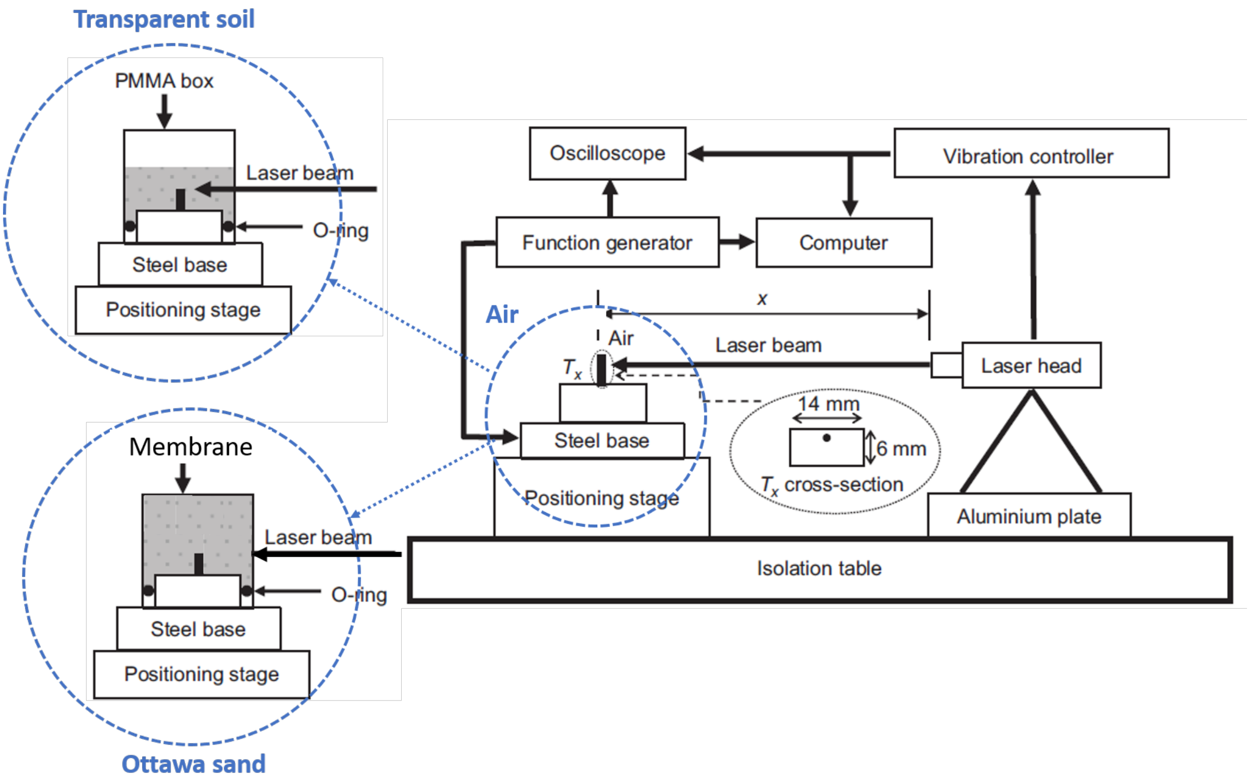

Figure 2: Configuration of the BE test and the laser vibrometer apparatus

The BE response under a sinusoidal electrical impulse is monitored in the air through a laser vibrometer apparatus. Based on the response of the BE, a coupled piezoelectrical-solid mechanics finite element model is calibrated so that the numerical prediction fits with the laser vibrometer measurements. The calibrated model in air is then verified against the laser vibrometer readings in a transparent soil. In the end, the calibrated model is used to predict independent vibrations induced by the BE motion within an Ottawa sand specimen under a confining pressure of 100 kPa. The soil parameters determined through trial and error from the FE model are then compared with the values obtained from a conventional RC test.

2.2. Experimental Tests

In the experimental BE tests shown in Figure 2, a function generator (model HP-33120A) generates the desired input voltage signal applied to the BE transmitter through the steel base. The signal is monitored by the oscilloscope (HP-54645A). The BE transforms the electrical energy into the mechanical energy, which then applies an ultrasonic impulse to the soil specimen. The BE transmitter used in this test protrudes 6 mm into the soil specimen and has a 14 mm by 1.0 mm cross section. The laser vibrometer (polytec, 2013) measures the displacement at a single point.

The measurements from the Ottawa sand specimen are used for the further verification of the proposed numerical model. The soil sample is 7.0 cm in diameter and 14 cm in height. The density of the dry sand is 1,848 kg/m^3. The soil specimen is slightly compacted and covered with a latex membrane to hold the sand in place. A 100 kPa vacuum pressure is applied at the bottom of the sand specimen. The vibration introduced by the BE transmitter was captured through the laser vibrometer on the wall of the soil specimen membrane, as shown in Figure 3. The measurements along the specimen are taken for every 1 cm. A reflective adhesive tape is applied to the membrane wall to improve the signal intensity.

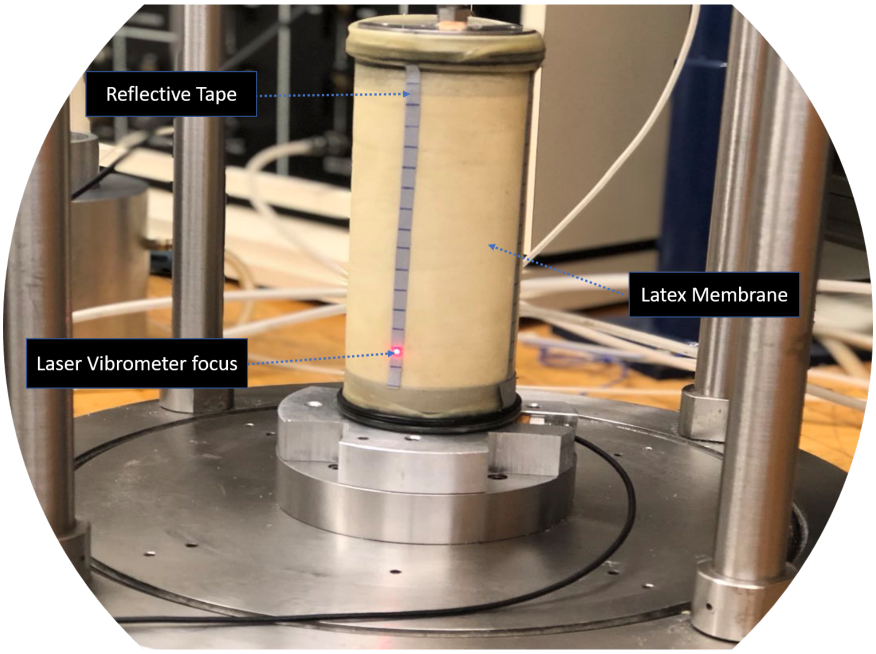

Figure 3: Vibration measurements through the laser vibrometer for the Ottawa sand specimen

Furthermore, the resonant column test, as shown in Figure 4, is performed based on the ASTM standard [2] for verification of the BE measurements at 100 kPa. The built-in source in the spectrum analyzer (HP-35670A) is used to apply a sinusoidal sweep input voltage. Due to the limited power in the spectrum analyzer, the power amplifier (Bogen GS-250) is used to amplify the input voltage. Such input current introduces the vibration of the magnets, which in turn induce a torsional excitation in the soil sample. The response of the specimen is recorded in terms of acceleration via the accelerometers (PCB353A78 and PCB 353B65) mounted on the driving plate. The current in the coils and the acceleration are amplified and filtered (200 Hz low pass) using a filter amplifier (KrohnHite 3384) before being processed by the spectrum analyzer for the transfer function calculations. The spectrum analyzer calculates the transfer function in real time. The resonance frequency and damping ratio of the soil specimen are computed from the transfer function.

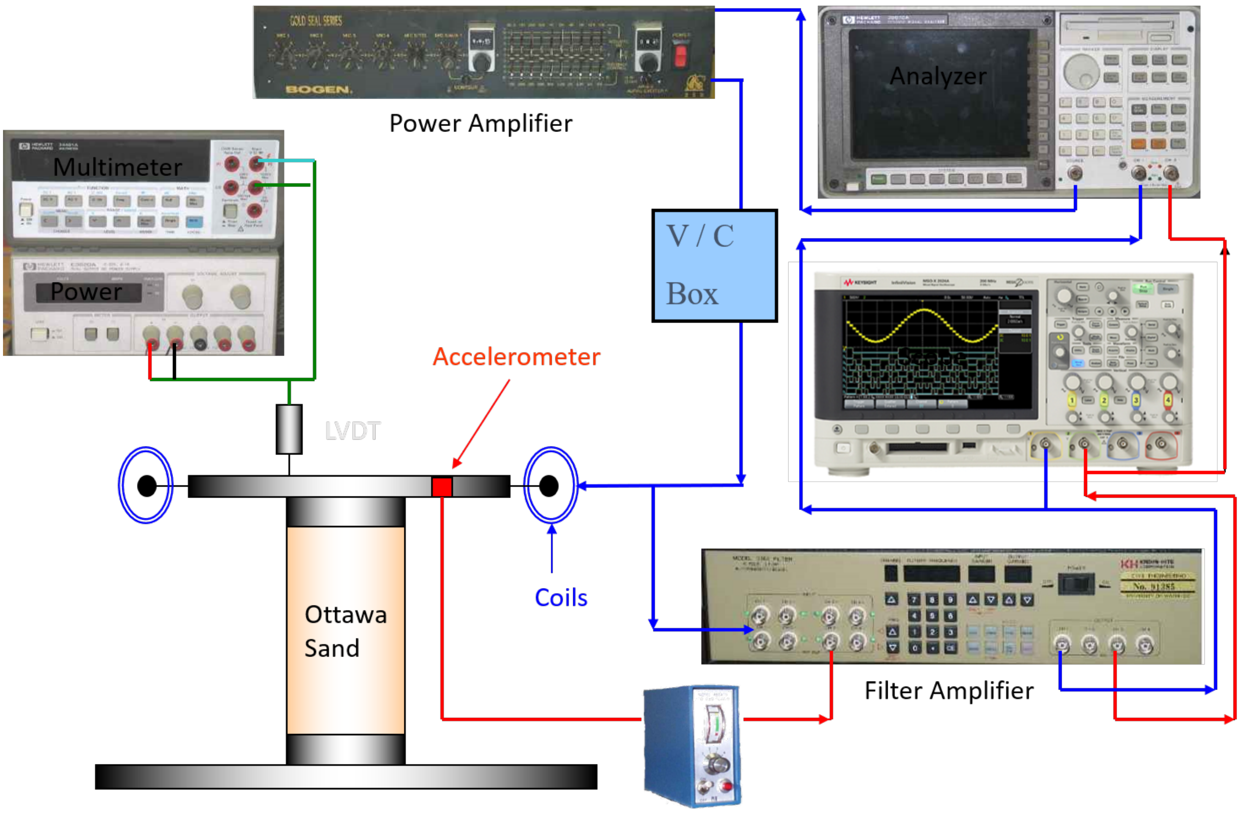

Figure 4: RC test setup for the measurement of shear wave and damping ratio

3. Theoretical Background

The motion of the BE in different media can be numerically simulated using a piezoelectric-solid mechanics theoretical framework. Also, the soil is considered as a solid, isotropic, and homogeneous medium. This framework can be then implemented in a FE numerical tool for further analyses. In this section, we will briefly review the assumptions and field equations. The FE modeling is then discussed.

3.1. Kinematic Assumptions

The linearized form of the Green-Lagrange strain tensor, ε_{ij}, for infinitesimal deformations of solid media (BE and soil) and electrical field E_i^f are described, respectively, as follows [21].

$$\begin{aligned} \varepsilon_{ij} &= \frac{1}{2}\left(u_{i,j} + u_{j,i}\right) \\ E_i^f &= -\phi_{,i} \end{aligned} \tag{1}$$

where $u_{i,j}$ represents $\frac{\partial u_i}{\partial x_j}$; u_i represents the displacement vector components of the solid medium in each direction and x_j represents the coordinates; E_i^f denotes the electrical field vector; ϕ is the electric potential.

3.2. Constitutive Models

The constitutive models that describe the stress-strain and electrical displacement-field relationships are defined as:

$$\begin{aligned} \sigma_{ij} &= C_{ijkl}\ \varepsilon_{kl} - e_{kij}E_k \\ D_i &= e_{ikl}\varepsilon_{kl} + \epsilon_{ik}E_k \end{aligned} \tag{2}$$

where σ_{ij} is the stress tensor; e_{kij} and ϵ_{ik} denote the piezoelectric tensor and dielectric permittivity tensor, respectively. D_i represents the electrical displacement. C_{ijkl} is the fourth-order linear elastic stiffness tensor described in Equation 3 for isotropic materials [19, 20]:

$$C_{ijkl} = \lambda\delta_{ij}\delta_{kl} + \mu\left(\delta_{ik}\delta_{jl} + \delta_{il}\delta_{jk}\right) \tag{3}$$

where $C_{11} = C_{33} = \frac{E'(1-\nu)}{(1+\nu)(1-2\nu)}$; $C_{12} = C_{13} = \frac{E'\nu}{(1+\nu)(1-2\nu)}$; $C_{44} = C_{55} = C_{66} = \frac{E'}{2(1+\nu)}$; E' and μ are Young's modulus and Poisson's ratio, respectively. It is worth mentioning that the stress-strain relationship for soils can be written as $\sigma_{ij} = C_{ijkl}\varepsilon_{kl}$. Also, the piezoelectric tensor e_{ijk} (coulomb/m^2) is written as [23]:

$$e = \begin{Bmatrix} 0 & 0 & 0 & 0 & e_{15} & 0 \\ 0 & 0 & 0 & e_{15} & 0 & 0 \\ e_{31} & e_{31} & e_{33} & 0 & 0 & 0 \end{Bmatrix} \tag{4}$$

Piezoelectric materials have the ability to produce an electrical voltage with an applied load; vice versa, motions are generated if an electric field is applied. Such phenomena is described through the piezoelectric tensor.

3.3. Conservation Laws

Conservation of the linear momentum for a solid medium (BE and soil) is written as:

$$\sigma_{ij,j} = \rho \ddot{u}_i \tag{5}$$

where ρ is the bulk density.

Gauss's law is used to describe the conversation of charge in the piezoelectric BE:

$$D_{i,i} = 0. \tag{6}$$

3.4. Field Equations

The governing equations for the BE can be written in terms of the displacement vector u_i as well as the electric field vector E_i^f as:

$$\begin{aligned} \mu u_{i,jj} + (\lambda + \mu) u_{j,ji} - e_{kij,j} E_k^f &= \rho \ddot{u}_i \\ e_{ikl,i} \varepsilon_{kl} + \epsilon_{ik,i} E_k^f &= 0. \end{aligned} \tag{7}$$

It should be noted the field equation 7 is obtained through the conservation of momentum and the conservation of charge, respectively. The coupled field equations are then solved simultaneously due to the coupling tensor e_{ikl}, which represents the inherent properties of the piezoelectric materials.

Similarly, the field equation governing the propagation of stress waves into the soil specimen due to the piezoelectric BE motion can be written as

$$\mu u_{i,jj} + (\lambda + \mu) u_{j,ji} = \rho \ddot{u}_i. \tag{8}$$

3.5. Finite Element Modeling and Boundary Conditions

The 2D FE method is used to solve the field equations described above via COMSOL Multiphysics [5]. The triangular element type is used for the analysis. The direct solver is used instead of an iterative solver due to its robust nature [18]. There are 5,145 elements with an average quality of 0.8592 (length to width ratio). Based on a extensive mesh sensitivity analysis, it is found that the numerical results are no longer sensitive to the mesh size if a finer mesh is used. With such settings in COMSOL Multiphysics, the relative error can be controlled to an acceptable tolerance. The mesh distribution in the soil specimen and BE is shown in Figure 5.

The BE having a height of 6 mm, a length of 14 mm, and a width of 1.0 mm is shaped as a cantilever beam and contains two layers of piezoelectric ceramic plates with a metal plate in the middle. If the poling direction of these two layers of piezoelectric elements is in the same direction, it would be called parallel and if the poling direction is in opposite directions, it would be called series type. The parallel type needs a low voltage to work, but the series type needs, for the same application, twice the voltage magnitude to work [29, 22]. The parallel BE is used as an transmitter and the series type is used as a receiver [29, 22]. The Ottawa sand specimen has a width of 70 mm and a height of 140 mm.

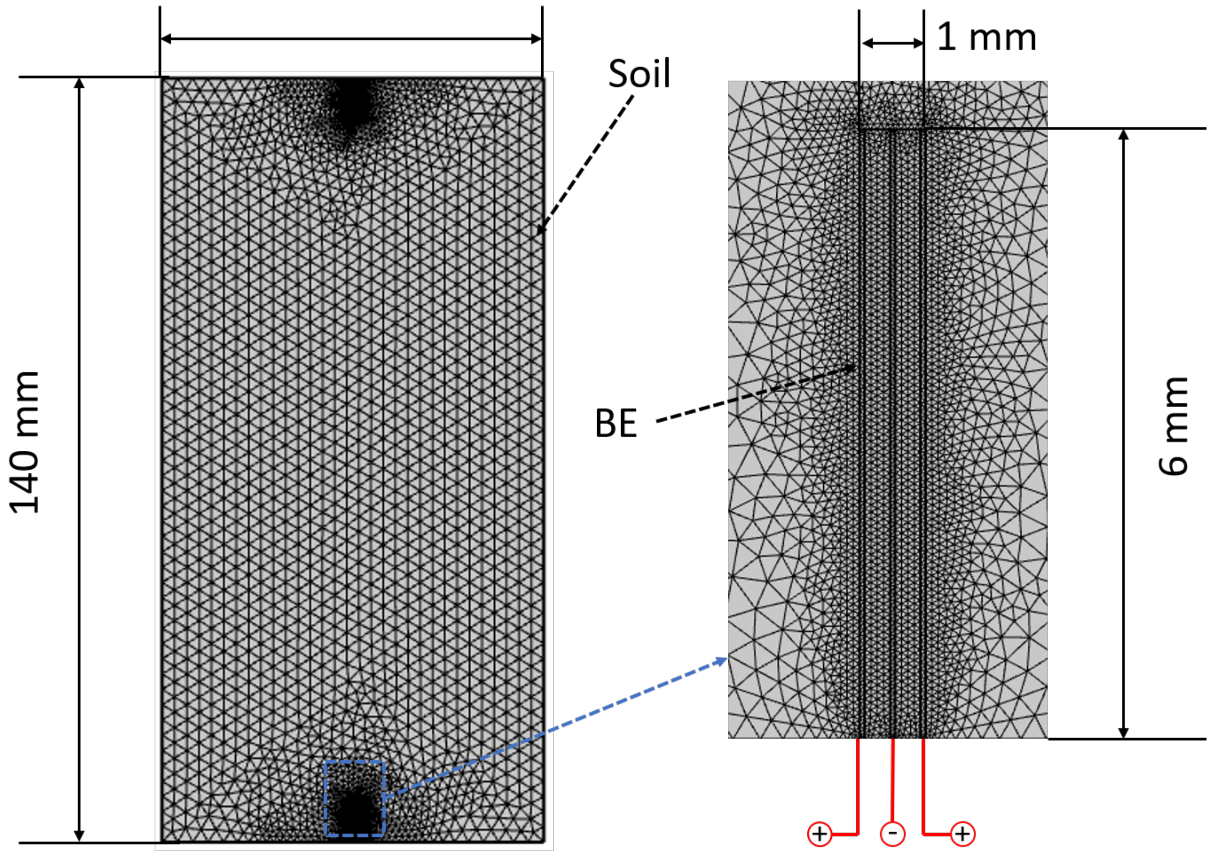

Figure 5: Mesh distribution for the BE test

A sinusoidal impulse voltage with a frequency of 9 kHz, which is close to the resonant frequency of the BE used in our tests, is applied to the BE (plus sign in Figure 5). A fixed boundary condition is applied to the top and bottom of the soil specimen. A fixed boundary condition is also applied to one end of the BE transmitter (lower end) and receiver (upper end). The remaining boundaries are considered as a free surface (zero stress) to allow the reflection of stress waves. The interface between the BE and surrounding soil is modeled by meeting the continuity conditions. The initial displacement and velocity of the BE and surrounding soils are set to be zero. The components of the coupling tensor in Equation 4 has the following values: $e_{31} = -5.35$ C/m^2; $e_{15} = 15.78$ C/m^2 and $e_{33} = 12.29$ C/m^2 [23]. The density of the piezoelectric ceramic plates used in the BE structure is 7,870 kg/m^3. The mechanical properties of the piezoelectric ceramic plates and the metal plate used in the BE structure, transparent soil and Ottawa sand are obtained through the calibration procedure by trial and error as presented in Section 4.1 and Section 4.2.

4. Results and Discussion

4.1. BE Motion Calibration and Verification

The laser pointer is concentrated at a point with a height of 5 mm shown in Figure 2. The comparison of the BE motion in the air between the experimental measurements and numerical predictions in time and frequency domains is shown in Figures 6a and 6b, respectively. As can be seen in Figure 6, the numerical results using the calibrated piezoelectric-solid mechanics model are in good agreement with the experimental measurements.

The mechanical properties of the BE are calibrated through trial and error to best fit the numerical predictions with the laser measurements. The best matching between the numerical results and the laser measurements was achieved when Young's modulus and Poisson's ratio of the piezoelectric ceramic plates are 65 GPa and 0.3, respectively; Young's modulus of the metal plate used in the BE structure is 243 GPa; and, the damping ratio for the piezoelectric ceramic plates and the metal plate used in the BE structure is 2.5%.

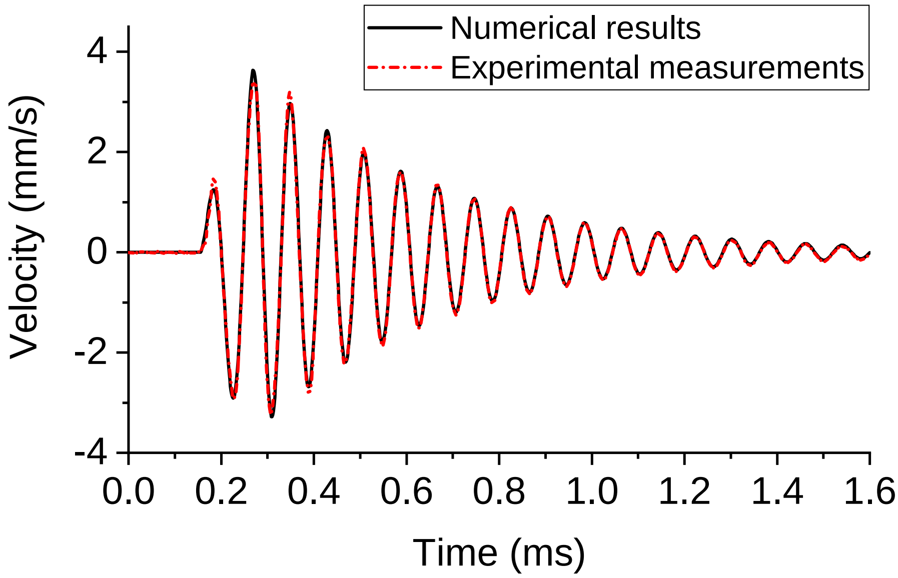

(a) time domain

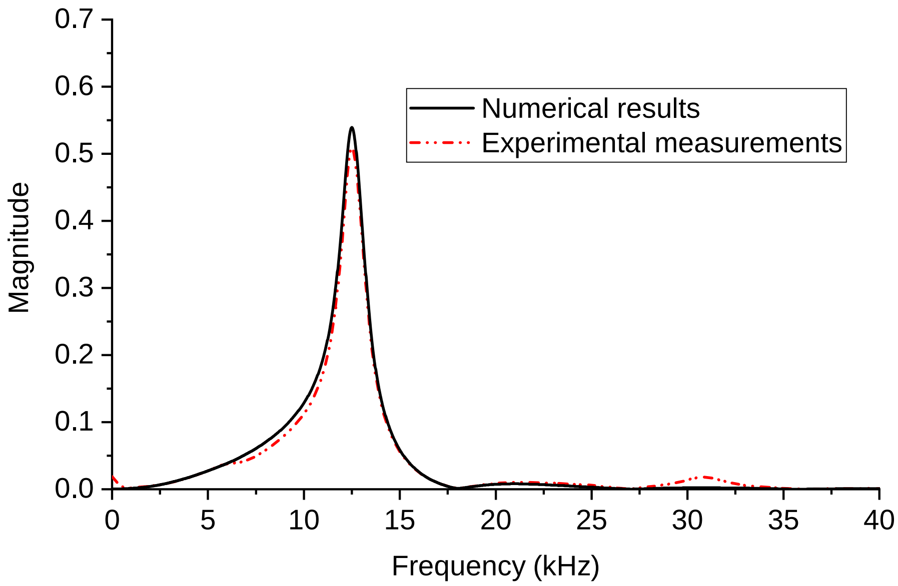

(b) frequency domain

Figure 6: Comparison between the experimental measurements and numerical results for the BE motion in the air in (a) time domain, (b) frequency domain.

The calibrated FE model is further verified through the experimental BE tests on the transparent soil (made of silica and oil) where the BE motion was monitored via the laser vibrometer. Under the same impulse voltage, the comparison between the numerical FE results and the experimental measurements of the BE motion are shown in Figure 7 in time and frequency domains.

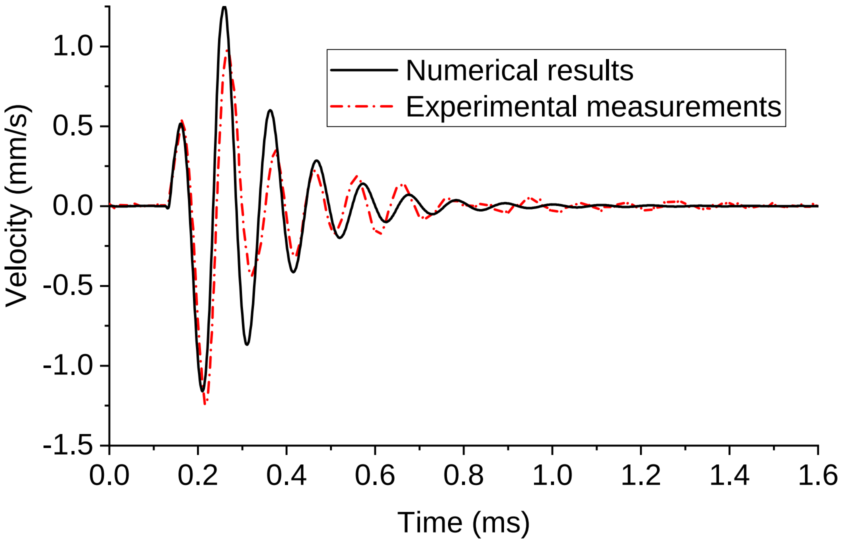

(a) time domain

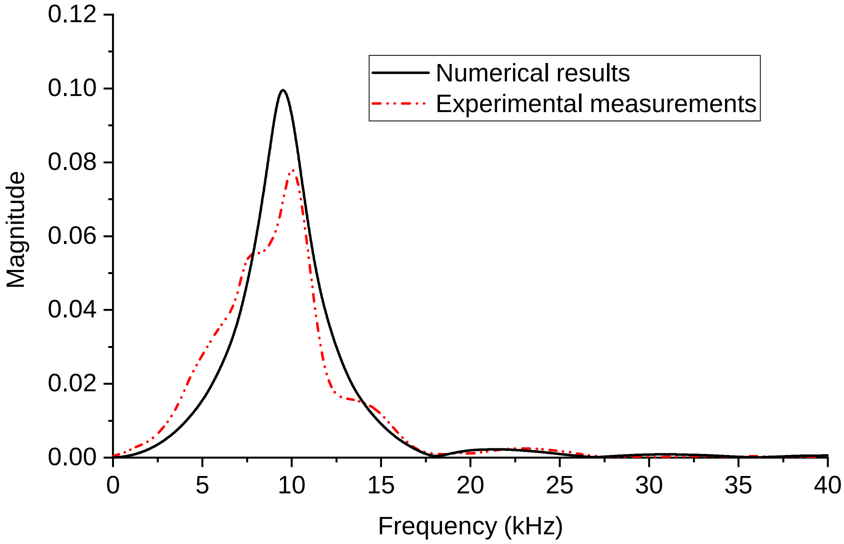

(b) frequency domain

Figure 7: Comparison between the experimental measurements and numerical results for the BE motion in the transparent soil in (a) time domain, (b) frequency domain.

The mechanical properties of the transparent soil used in the FE analysis are calibrated by trial and error. It is found that the speeds of the P wave and S wave in the transparent soil studied in this test are approximately 1,200 m/s and 15 m/s, respectively. The equivalent damping ratio of the transparent soil including the visco-elastic effect is assumed as 0.3. This damping value is high because it is representing not only the damping of the soil, but also the effect of the added mass of the transparent soil to the response of the BE Irfan et al. [14]. The very low shear wave velocity derived numerically is due to the fact that the confining pressure is practically zero in this experiment. The high value of the P-wave velocity is generated because of the saturated conditions. The calibrated piezoelectric-solid mechanics model for the BE motion is still able to capture the motion of the BE in the transparent soil.

4.2. BE Motion in Ottawa Sand

The BE motion can be directly monitored in the air and transparent soil through the laser vibrometer since the laser light can penetrate into these media. It is not, however, the case for the BE test performed on real soils. Therefore, the displacement at the sides of the soil specimen is monitored instead of the BE itself. The setup for this test can be seen in Figure 3. The original laser measurements at the elevations of 2.5 cm (trace 0) to 13.5 cm (trace 12), with an interval of 1 cm, are shown in Figure 8. This signal is contaminated with the higher resonant modes of the BE motion [17]. Since the applied voltage signal is 9 kHz, the components above 15 kHz are removed through the wavelet synchrosqueezed transform [6]. The components below 15 kHz are obtained through the inverse wavelet synchrosqueezed transform.

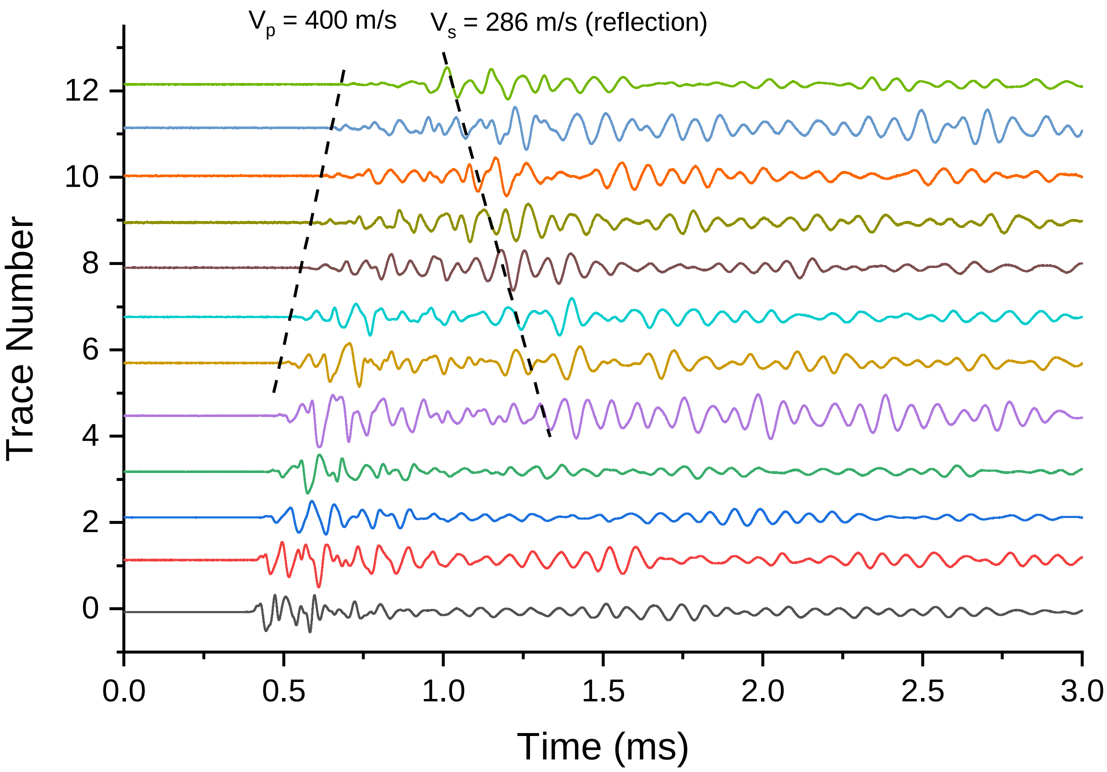

Figure 8: Original displacement measurement along Ottawa sand specimen using the laser vibrometer

Based on the calibrated piezoelectric-solid mechanics model for the BE, the soil parameters are then modified through trial and error to match the filtered laser vibrometer measurements. For example, the comparison between typical numerical and experimental displacements is shown in Figure 9. The best fitting was achieved by using the shear wave velocity of 240 m/s, compression wave velocity of 380 m/s (equivalent to a Young's modulus of 249 MPa and a Poisson's ratio of 0.17), and a damping ratio of 1% for the Ottawa sand. The determined P and S wave velocities can also be verified from the original laser measurements. Two constant slopes (400 m/s and 286 m/s slope) are also clearly visualized in the original displacement measurements, as labeled in Figure 8. The determined P wave velocity (380 m/s) and S wave velocity (240 m/s) were relatively close to the P wave velocity (400 m/s) and S wave velocity (286 m/s) visualized in the original laser measurements.

Furthermore, the dispersion curves were also computed using the numerical and measured displacement data. Figure 10 shows the comparison between the measured and numerical dispersion curves for both symmetric and antisymmetric modes. The numerical predictions showed a reasonable agreement with the laser measurements in terms of the distribution of dispersion curves. Therefore, the P wave and S wave velocity for the Ottawa sand are 380 m/s and 240 m/s, which is verified through comparison in displacement measurements and dispersion curves.

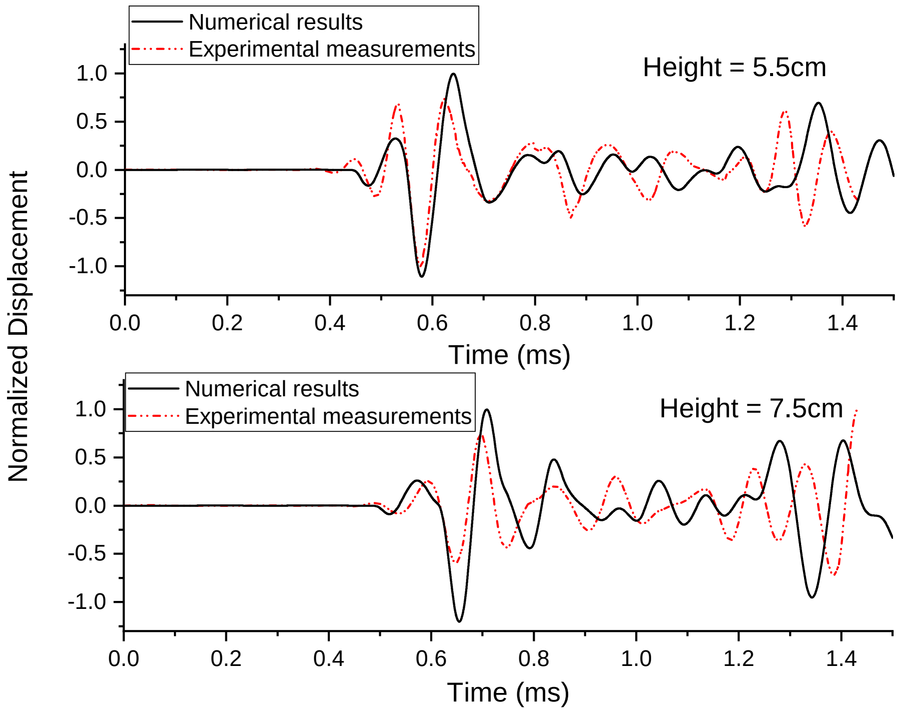

Figure 9: Comparison between the numerical results and experimental displacement measured at a distance of 5.5 and 7.5 cm from the bottom

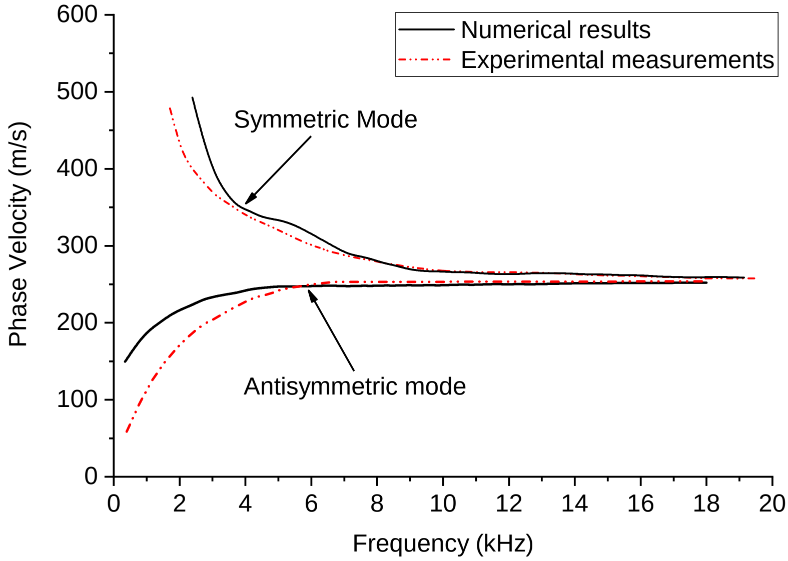

Figure 10: Comparison between the numerical and experimental dispersion curves

The BE motion at different heights (1 mm, 3 mm, and 5 mm) within the Ottawa sand specimen is shown in Figure 11. The first cycle in the signals is introduced by the applied voltage due to the piezoelectrical effects. The vibrations after the first cycle in the signals are due to the free vibration of the BE and wave reflection within the soil specimen. However, the BE motion is mostly dominated by the applied voltage (first cycle). Figure 11 also shows the deformation of the BE. The predominant vibrating frequency and period of the BE transmitter is 8.7 kHz and 0.115 ms, respectively in the Ottawa sand specimen. In the first 1/4 period, the left piezoelectrical plate is moving relatively upward, which drives the BE to move to the left side. Such a phenomenon was already known in Fredy [10] and the proposed piezoelectric-solid mechanics model can describe it physically and qualitatively. BE does not only have the first mode of vibration under the applied electrical impulse. As shown in Figure 11, the BE exhibited the second mode of vibration after 0.06 ms (1/2 period) since the beginning of the impulse load.

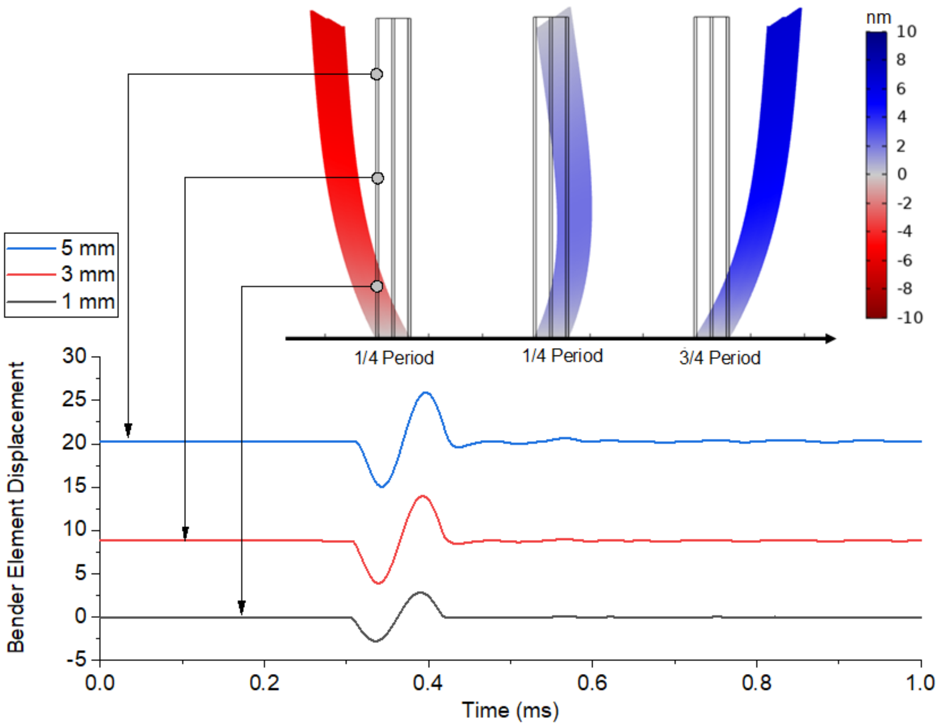

Figure 11: BE transmitter motion numerically predicted at different heights

4.3. Wave Analysis within Soil Specimen

The wave propagation is further analyzed through the displacement distribution within the Ottawa sand specimen. The transmitter started the generation of mechanical energy around $t = 0.31$ ms. This reference value is shown by *Trigger Point* in Figure 12.

The S wave velocity determined by the BE is relatively higher than the value obtained by the standard RC test Fam et al. [8]. The S wave velocity in the BE test is commonly calculated as distance divided by the S wave arrival time. However, the arrival time of the S wave is normally empirically selected around the first peak in the output signal. Based on the determined S wave velocity from previous discussion, the exact S wave arrival time can be located around 0.53 ms relative to the beginning of impulse (as labeled by Trigger Point in Figure 12). The measured response in BE testing is given in terms of voltage (Volts) while the numerical response is given by displacement (nm). These two signals are not expected to be identical as the received signal does not have units of displacement, velocity, or acceleration. The comparison between the measured and numerically calculated signal at the BE receiver location is shown in Figure 12. A reasonable agreement between the numerical results and experimental data is achieved. The S wave arrival time is normally selected shortly before the peak in the BE receiver signal. However, it is shown that the S wave arrival time is actually affected by the interaction with the p-wave. Therefore, the proposed numerical model can be used to improve the interpretation of the effects of p-waves on BE tests results.

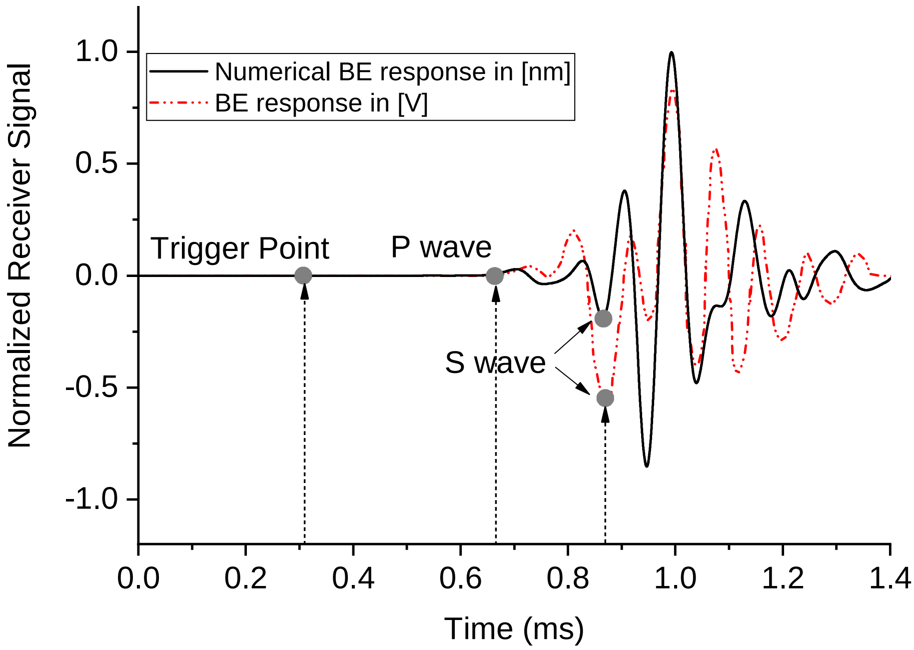

Figure 12: Comparison between experimental data and numerical results at the BE receiver location (this figure shows a relative comparison; the BE signals are not linearly related to vibration measurements such as displacement, velocity, or acceleration.)

The horizontal displacement contours corresponding to travel times equal to one up to five excitation periods are shown in Figure 13. The positive and negative displacements are shown in blue and red colors, respectively. A full wavelength is defined by a positive (red) and negative displacement (blue) wavefronts. For the dominant frequency of 8.7 kHz for the BE vibration in Ottawa sand, the S and P waves' wavelengths can be calculated as $\lambda_s = 2.8$ cm and $\lambda_p = 4.4$ cm, respectively. Two wavelengths are identified due to the different propagation speeds of P and S waves. In the BE test, the generation of the S wave mode (in terms of its amplitude) is much stronger than that of the P wave mode. Only a half wavelength (blue front) was identified for the P wave mode due to its weaker generation in the BE test. Furthermore, P wave attenuates with travelling distance and the identification of its full wavelength becomes impractical. Therefore, only a half wavelength of the P wave mode is labeled in Figure 13. After the first period (1T), the reflection of P and S waves can be visualized clearly. The separation between the P wave and S wavefronts increased from the 2^{nd} and 3^{rd} periods. The P wavefront arrives at the BE receiver tip sometime between the 3^{rd} and 4^{th} periods. Similarly, the S wavefront arrives at the BE receiver tip sometime between the 4^{th} and 5^{th} periods.

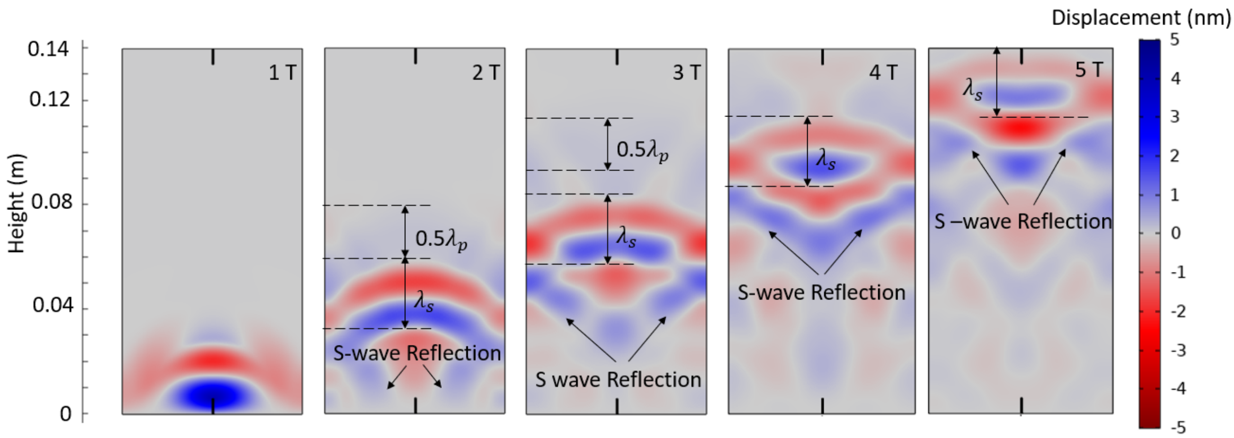

Figure 13: Horizontal displacement contour in Ottawa sand

4.4. Comparison with RC Test

The RC test was performed to validate the shear wave velocity and damping ratio of the Ottawa sand under various confining pressures, as shown in Figure 14 and Figure 15, respectively. As the confining pressure increases, the soil specimen gradually gains more strength, which results in an increase in the shear wave velocity. On the other hand, the increasing confining pressure constrains the movement of soil particles, which is shown as a reduction in damping ratio.The relation between shear wave velocity (v_s) and confining pressure (σ_0) for RC test results can be expressed as : $v_s = 93.9\ \sigma_0^{0.22}$. Similarly, the relation for damping ratio (ξ) and and confining pressure (σ_0) for RC test results is expressed as: $\xi = 407.3\ \sigma_0^{-1.26}$. Under a confining pressure of 100 kPa, the shear wave velocity and damping ratio are found to be 263 m/s and 1.06%, which are consistent with the values used in the numerical model through trial and error.

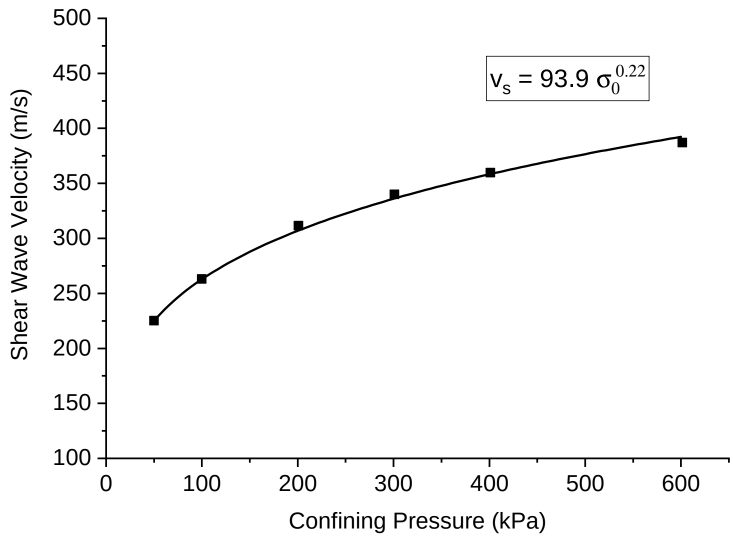

Figure 14: Shear wave velocity measured by the resonant column test on Ottawa sand under various confining pressures

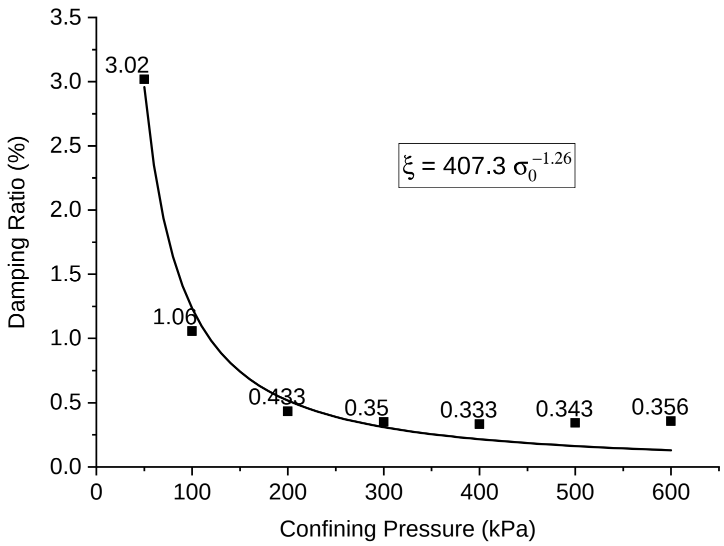

Figure 15: Damping ratio measured by the resonant column test on Ottawa sand under various confining pressures

4.5. Numerical Study of the Effect of Different Poisson's Ratios (Loose Sand, Soft Clay)

The wave propagation is also investigated in two different soil specimens using the piezoelectric-solid mechanics FE model. In Case 1, the P and S wave velocities are 120 m/s and 69.3 m/s (equivalent to a Young's modulus of 22 MPa and a Poisson's ratio of 0.25) to simulate a loose sand specimen. In Case 2, a soft clay soil sample with a P wave velocity of 120 m/s and an S wave velocity of 35.2 m/s (equivalent to a Young's modulus of 6.7 MPa and a Poisson's ratio of 0.45) is studied. The horizontal displacements at the BE receiver location are shown in Figure 16 for Case 1 and Case 2. The exact P wave travel time is 1.07 ms relative to the beginning of the impulse as labeled by Trigger Point. In Case 1, the exact S wave travel time is 1.85 ms relative to the beginning of the impulse. Similarly, in Case 2, the S wave travel time is 3.63 ms.

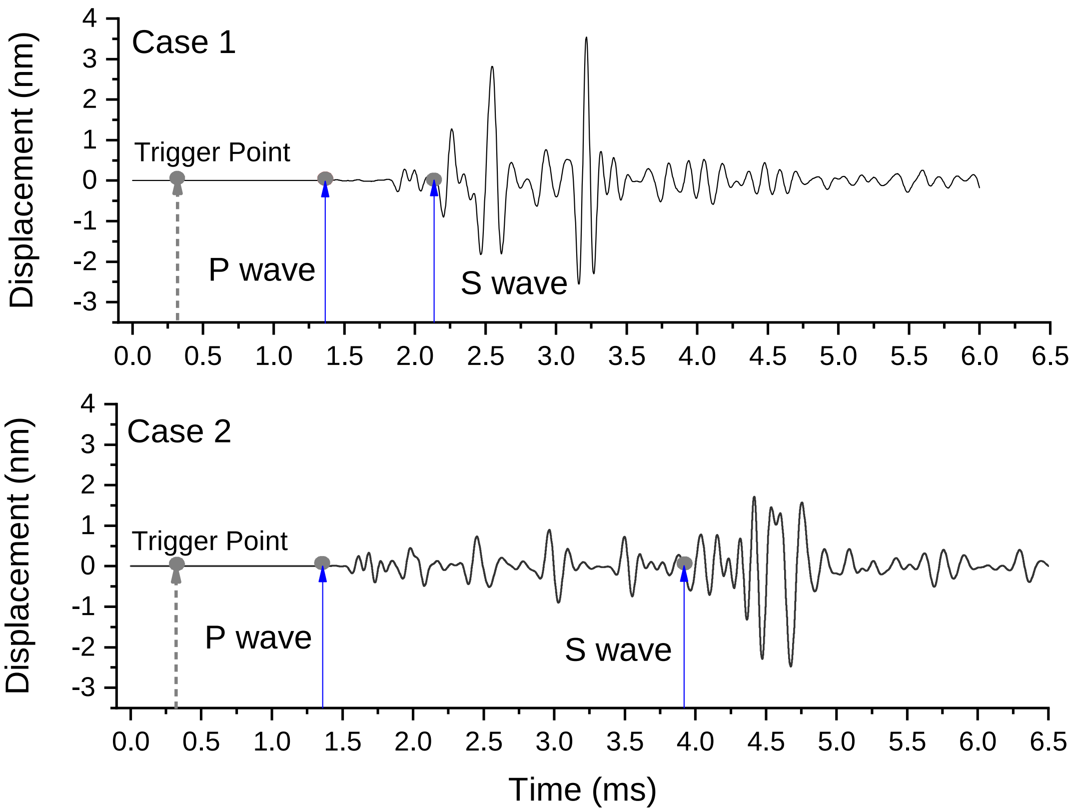

Figure 16: Horizontal displacement at the receiver location for Case 1 (Poisson's ratio = 0.25, loose sand) and Case 2 (Poisson's ratio =0.45, soft clay)

The signal obtained in Case 2 is more contaminated by the P wave because of its slower S wave velocity. The components located between the first P wave arrival time (1.37 ms) and first S wave arrival time (3.94 ms) are due to the P wave reflection from the sides of the soil specimen, as illustrated in Figure 18. In this case, the selection of the S wave arrival time is rather challenging and unpredictable based on the empirical methods. However, the real arrival time of the S wave is not closely near to the largest amplitude, as shown in Figure 16.

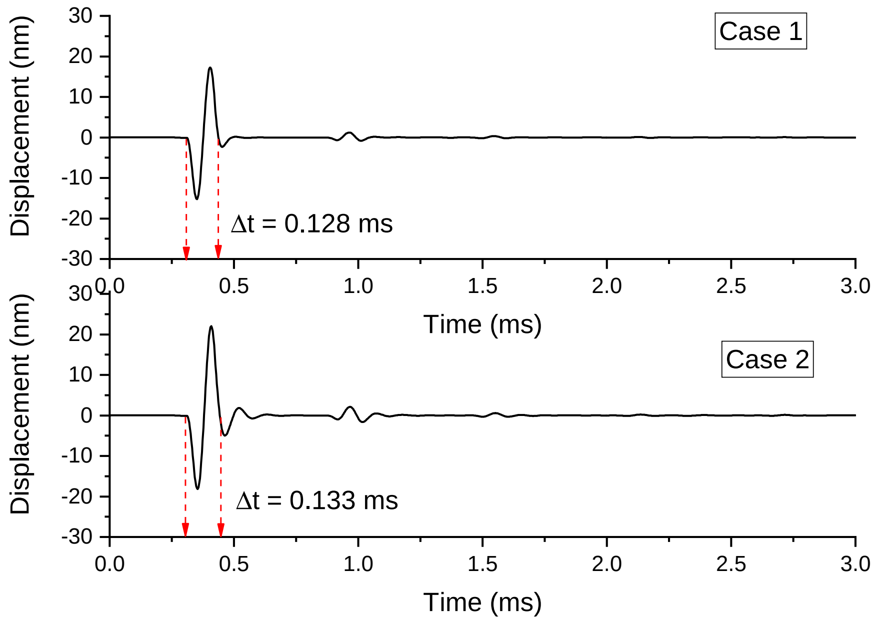

Figure 17: Horizontal displacement of BE transmitter numerically predicted at a height of 5mm for Case 1 (Poisson's ratio = 0.25, loose sand) and Case 2 (Poisson's ratio =0.45, soft clay)

The horizontal displacement of BE transmitter is shown in Figure 17 for both Case 1 and Case 2. From Figure 17, it is found that BE transmitter vibrates with the dominant frequency of 7.8 kHz for the BE vibration in Case 1. Corresponding, the S and P waves' wavelengths can be calculated as $\lambda_s = 0.89$ cm and $\lambda_p = 1.5$ cm, respectively. In Case 2, the dominant frequency of the BE motion is 7.5 kHz and the S and P waves' wavelengths can be calculated as $\lambda_s = 0.47$ cm and $\lambda_p = 1.6$ cm, respectively. The displacement contours at different times (normalized in terms of period) are shown in Figure 19 and Figure 18 for Case 1 and Case 2, respectively. It is confirmed from Figure 19 and Figure 18 that the reflected P waves from the sides of the specimen can arrive at the BE receiver location faster than the shear wavefront. Therefore, the wave interactions of P and S waves with soil boundaries can largely increase the complexity of the selection of the S wave arrival time. The traditional empirical methods cannot accommodate the complex nature of wave interaction and may result in misleading predictions of the S wave velocity.

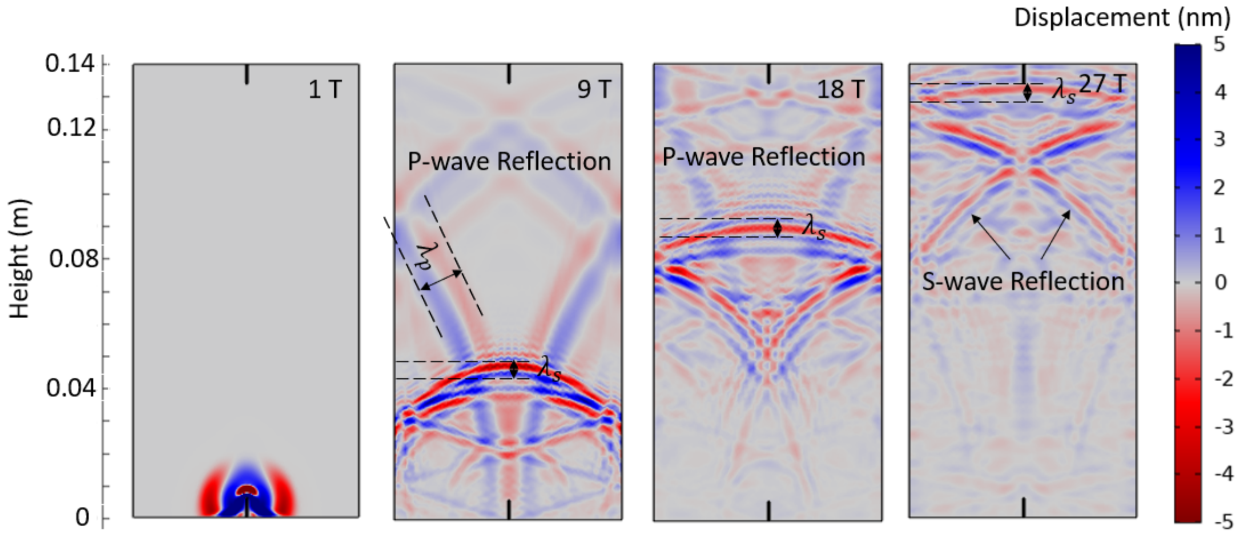

Figure 18: Horizontal displacement contour in low-stiffness clay for Case 2 (Poisson's ratio =0.45, soft clay)

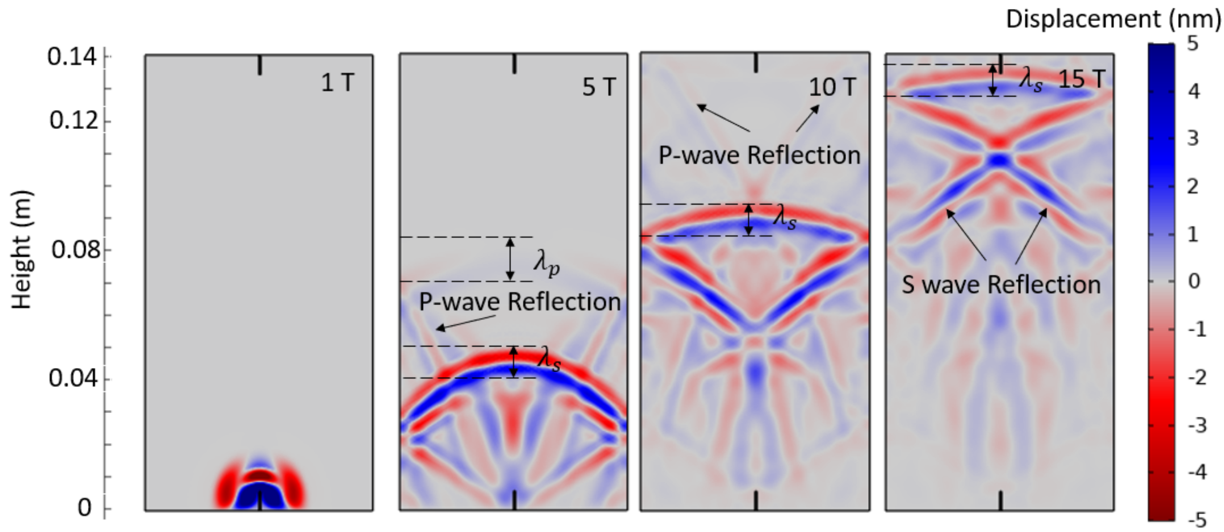

Figure 19: Horizontal displacement contour in low-stiffness sand for Case 1 (Poisson's ratio = 0.25, loose sand)

5. Conclusion

In this paper, the response of different media to a BE motion is thoroughly studied via a piezoelectric-solid mechanics FE model as well as experimental tests. The numerical results are compared with the motion of the BE in the air, transparent soil, as well as the Ottawa sand captured by a laser vibrometer. It is concluded that:

- The proposed piezoelectric-mechanical model captures the motion of the BE with sufficient accuracy in the air, transparent soil, as well as the Ottawa sand. The best agreement was achieved for the BE motion in the air.
- The numerical response obtained by the proposed model is consistent with the laser vibrometer measurement at the sides of the Ottawa sand specimen. Furthermore, the numerical predictions show a reasonable agreement with the laser measurements in terms of the distribution of dispersion curves for both symmetric and antisymmetric modes.
- A reasonable agreement between the numerical BE response and experimental BE measurement is achieved at the receiver location. The shear wave velocity and damping ratio obtained through the proposed model are consistent with the ones obtained by the resonant column test.
- The proposed numerical method shows that there is a significant p-wave/s-wave interaction that demonstrates why the empirical methods for the selection of s-waves in BE testing could be incorrect depending on the different parameters that affect the participation of p-waves.
- The proposed piezoelectric-mechanical model can be used to study the complex wave interactions, which significantly improves the interpretation of the effects of p-waves on BE test results. The proposed model clearly show that the interpretation of BE measurements in clays could be more challenging because of the strong participation of p-waves on the response of BE.

References

[1] Rajendram Arulnathan, Ross W Boulanger, and Michael F Riemer. Analysis of bender element tests. *Geotechnical Testing Journal*, 21(2):120–131, 1998.

[2] ASTM. Standard test methods for modulus and damping of soils by resonant-column method, 2007.

[3] Javier Camacho-Tauta, Juan David Jimenez Alvarez, and Oscar Javier Reyes-Ortiz. A procedure to calibrate and perform the bender element test. *Dyna*, 79(176):10–18, 2012.

[4] JF Camacho-Tauta, Giovanni Cascante, A Viana da Fonseca, and JA Santos. Time and frequency domain evaluation of bender element systems. *Géotechnique*, 65(7):548–562, 2015.

[5] AB Comsol. Comsol multiphysics reference manual. *Version*, 2007.

[6] Ingrid Daubechies, Jianfeng Lu, and Hau-Tieng Wu. Synchrosqueezed wavelet transforms: An empirical mode decomposition-like tool. *Applied and computational harmonic analysis*, 30(2):243–261, 2011.

[7] Robert Dunsch and Jean-Marc Breguet. Unified mechanical approach to piezoelectric bender modeling. *Sensors and Actuators A: physical*, 134(2):436–446, 2007.

[8] MA Fam, Giovanni Cascante, and MB Dusseault. Large and small strain properties of sands subjected to local void increase. *Journal of Geotechnical and Geoenvironmental Engineering*, 128(12):1018–1025, 2002.

[9] Mathieu Finas, Hassan Ali, Giovanni Cascante, and Philippe Vanheeghe. Automatic shear wave velocity estimation in bender element testing. *Geotechnical Testing Journal*, 39(4):557–567, 2016.

[10] Alonso Diaz Duran Fredy. Excitation force and frequency effects in wave-based techniques for the characterization of geomaterials at different scales. 2020.

[11] Xiaoqiang Gu, Jun Yang, Maosong Huang, and Guangyun Gao. Bender element tests in dry and saturated sand: Signal interpretation and result comparison. *Soils and Foundations*, 55(5):951–962, 2015.

[12] Laureano R Hoyos, Eduardo A Suescún-Florez, and Anand J Puppala. Stiffness of intermediate unsaturated soil from simultaneous suction-controlled resonant column and bender element testing. *Engineering Geology*, 188:10–28, 2015.

[13] R Ingale, A Patel, and A Mandal. Numerical modelling of bender element test in soils. *Measurement*, 152:107310, 2020.

[14] Muhammad Irfan, Giovanni Cascante, Dipanjan Basu, and Zahid Khan. Novel evaluation of bender element transmitter response in transparent soil. *Géotechnique*, pages 1–12, 2019.

[15] Vojkan Jovičić and MP Coop. The measurement of stiffness anisotropy in clays with bender element

tests in the triaxial apparatus. *Geotechnical Testing Journal*, 21(1):3–10, 1998.

[16] Lutz Karl, Wim Haegeman, Lincy Pyl, and Geert Degrande. Measurement of material damping with bender elements in triaxial cell. *Deformation Characteristics of Geomaterials*, pages 3–11, 2003.

[17] Jong-Sub Lee and J Carlos Santamarina. Bender elements: performance and signal interpretation. *Journal of geotechnical and geoenvironmental engineering*, 131(9):1063–1070, 2005.

[18] Hongwei Liu, Pooneh Maghoul, Ako Bahari, and Miroslava Kavgic. Feasibility study of snow melting system for bridge decks using geothermal energy piles integrated with heat pump in canada. *Renewable energy*, 136:1266–1280, 2019.

[19] Hongwei Liu, Pooneh Maghoul, Ahmed Shalaby, Ako Bahari, and Farid Moradi. Integrated approach for the masw dispersion analysis using the spectral element technique and trust region reflective method. *Computers and Geotechnics*, 125:103689, 2020.

[20] G Thomas Mase, Ronald E Smelser, and George E Mase. *Continuum mechanics for engineers*. CRC press, 2009.

[21] MA Matin, D Akai, N Kawazu, M Hanebuchi, K Sawada, and M Ishida. Fe modeling of stress and deflection of pzt actuated micro-mirror: Effect of crystal anisotropy. *Computational materials science*, 48(2):349–359, 2010.

[22] Sarju Mulmi, Takeshi Sato, and Reiko Kuwano. Performance of plate type piezo-ceramic transducers for elastic wave measurements in laboratory soil specimens. *Seisan Kenkyu*, 60(6):565–569, 2008.

[23] Oliver J Myers, M Anjanappa, and Carl B Freidhoff. Numerical modeling of a circularly interdigitated piezoelectric microactuator. *Journal of microelectromechanical systems*, 19(5):1098–1104, 2010.

[24] J O'Donovan, C O'Sullivan, and G Marketos. Two-dimensional discrete element modelling of bender element tests on an idealised granular material. *Granular Matter*, 14(6):733–747, 2012.

[25] V Rabbani, A Bahari, M Hodaei, P Maghoul, and N Wu. Three-dimensional free vibration analysis of triclinic piezoelectric hollow cylinder. *Composites Part B: Engineering*, 158:352–363, 2019.

[26] Giulia Viggiani and JH Atkinson. Interpretation of bender element tests. *Géotechnique*, 45(1):149–154, 1995.

[27] Jun-Ung Youn, Yun-Wook Choo, and Dong-Soo Kim. Measurement of small-strain shear modulus g max of dry and saturated sands by bender element, resonant column, and torsional shear tests. *Canadian Geotechnical Journal*, 45(10):1426–1438, 2008.

[28] Yan-guo Zhou, Yun-min Chen, and Hao-jiang Ding. Analytical modeling of sandwich beam for piezoelectric bender elements. *Applied Mathematics and Mechanics*, 28(12):1581, 2007.

[29] Yan-guo Zhou, Yun-min Chen, Hao-jiang Ding, and Wei-qiu Chen. Modeling of sensor function for piezoelectric bender elements. *Journal of Zhejiang University-SCIENCE A*, 9(1):1–7, 2008.